

One-Step Synthesis of Antioxidative Graphene-Wrapped Copper Nanoparticles on Flexible Substrates for Electronic and Electrocatalytic Applications

Chi-Ang Tseng,[†] Chiao-Chen Chen,[†] Rajesh Kumar Ulaganathan,[†] Chuan-Pei Lee,[†] Hsu-Cheng Chiang,[†] Chin-Fu Chang,[†] and Yit-Tsong Chen^{*†§ID}

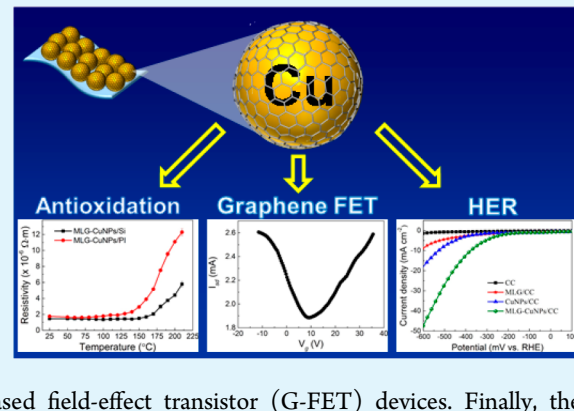
[†]Department of Chemistry, National Taiwan University, No. 1, Sec. 4, Roosevelt Road, Taipei 106, Taiwan

[§]Institute of Atomic and Molecular Sciences, Academia Sinica, P.O. Box 23-166, Taipei 106, Taiwan

Supporting Information

ABSTRACT: In this study, we report a novel, one-step synthesis method to fabricate multilayer graphene (MLG)-wrapped copper nanoparticles (CuNPs) directly on various substrates (e.g., polyimide film (PI), carbon cloth (CC), or Si wafer (Si)). The electrical resistivities of the pristine MLG-CuNPs/PI and MLG-CuNPs/Si were measured 1.7×10^{-6} and $1.4 \times 10^{-6} \Omega\text{-m}$, respectively, of which both values are ~ 100 -fold lower than earlier reports. The MLG shell could remarkably prevent the Cu nanocore from serious damages after MLG-CuNPs being exposed to various harsh conditions. Both MLG-CuNPs/PI and MLG-CuNPs/Si retained almost their conductivities after ambient annealing at 150°C . Furthermore, the flexible MLG-CuNPs/PI exhibits excellent mechanical durability after 1000 bending cycles. We also demonstrate that the MLG-CuNPs/PI can be used as promising source-drain electrodes in fabricating flexible graphene-based field-effect transistor (G-FET) devices. Finally, the MLG-CuNPs/CC was shown to possess high performance and durability toward hydrogen evolution reaction (HER).

KEYWORDS: antioxidation, copper nanoparticle, graphene, field-effect transistor, hydrogen evolution reaction



Metal nanoparticles with unique electrical and catalytic properties attracted vast attention in the past decades and have been used for a variety of applications, such as the electrodes for field-effect transistors,¹ organic solar cells,² surface-enhanced Raman scattering,^{3,4} and hydrogen evolution reactions (HER).⁵ In particular, the noble metals, such as gold (Au) and platinum (Pt), have drawn enormous interest due to their high electrical conductivity, excellent oxidation resistivity and prominent electrochemical activity.⁶ However, the high cost of these noble metals has hindered them from practical applications. Therefore, the synthesis of low-cost and earth-abundant metal nanoparticles with superior electrical conductivity and oxidation resistivity has drawn increasing interest in both fundamental research and industrial applications.

Copper nanoparticles (CuNPs) are considered to be a promising candidate to replace most noble metals due to their relatively low cost, nontoxic element and high electrical conductivity. However, when exposing to a room-temperature ambient condition within hours, bare CuNPs are subjected to easy oxidation to form nonconductive copper oxides, which could result in severe degradation in electrical conductivity.⁷ Consequently, how to prevent CuNPs from oxidation to maintain their excellent electrical conductivity is a prerequisite for advanced electronic and electrocatalytic applications.

Graphene, a monolayer of carbon atoms tightly packed into a two-dimensional (2D) honeycomb lattice, has displayed great potential in wide applications,^{8–11} especially for the encapsulation of CuNPs to fabricate flexible electronics because of its exceptional electrical conductivity, impermeability,¹² chemical stability, and high mechanical strength.¹³ For electrode applications, multilayer graphene-encapsulated copper nanoparticles (referred to as MLG-CuNPs) can be designed to protect the enclosed Cu nanocores from oxidation¹⁴ and simultaneously to serve as a conductive contact between individual MLG-CuNPs to maintain electrical transport.¹⁵ Several efforts have recently been reported to synthesize MLG-CuNPs. Lee et al.¹⁶ prepared MLG-CuNPs at 800–900 °C by using solid-phase poly(methyl methacrylate) as a carbon source and found that the solid-phase carbon source can also protect CuNPs from agglomeration during the synthesis. Wang et al.¹⁷ successfully synthesized MLG-CuNPs at 600 °C by using copper(II) acetylacetone ($\text{Cu}(\text{acac})_2$) as a reaction precursor and proposed a coalescence mechanism for the formation of MLG-CuNPs. First, the gaseous $\text{Cu}(\text{acac})_2$ decomposed at high temperature and created Cu vapor to

Received: May 9, 2017

Accepted: July 20, 2017

Published: July 20, 2017



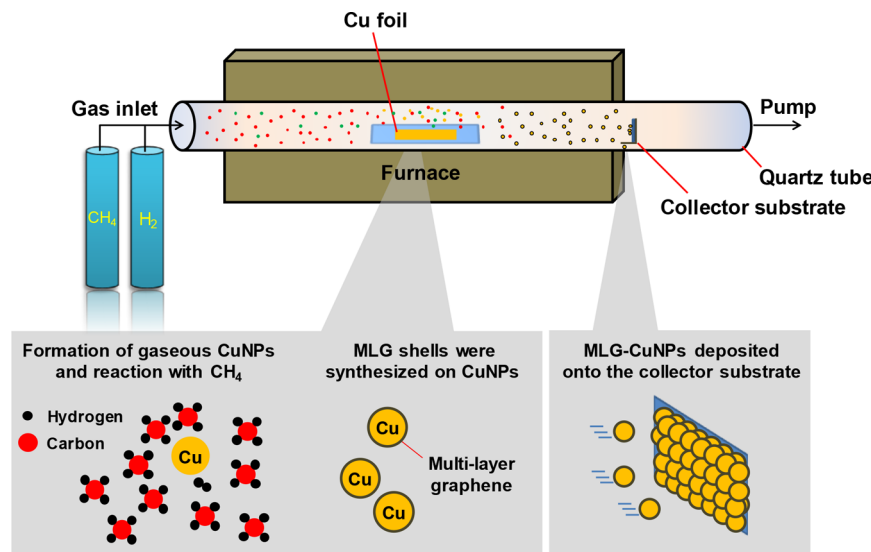


Figure 1. Schematic representation illustrates the experimental setup for the growth of MLG-CuNPs in CVD reaction. A growth mechanism of the as-synthesized MLG-CuNPs is proposed in the lower panels.

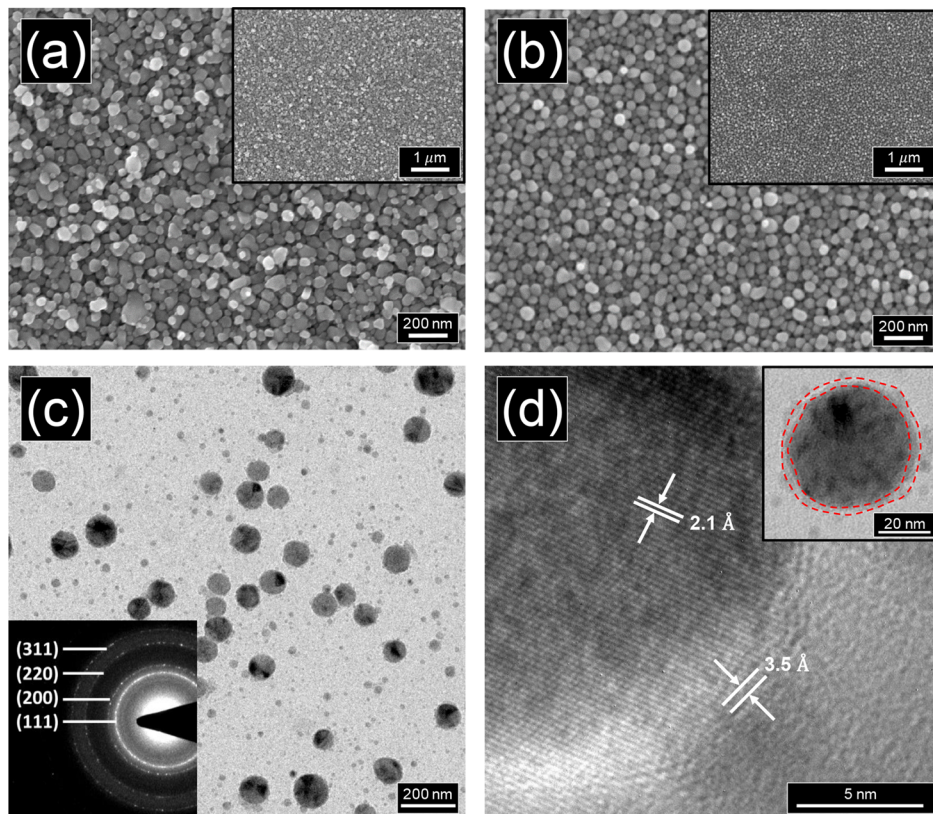


Figure 2. High-magnification SEM images of the as-synthesized (a) MLG-CuNPs/Si and (b) MLG-CuNPs/PI. The insets present the corresponding low-magnification SEM images. (c) TEM image of MLG-CuNPs. The inset displays the SAED pattern of the face-centered cubic (FCC) CuNPs. (d) HR-TEM image of a MLG-CuNP reveals the interlayer spacing (3.5 \AA) of graphene and the interplanar distance (2.1 \AA) of Cu(111). The inset displays the image of a MLG-CuNP with a $\sim 3 \text{ nm}$ -thick MLG shell.

form stable Cu nanoclusters. The Cu nanoclusters acted as a catalyst to facilitate the further decomposition of acetylacetone radicals and the subsequent adsorption of carbon atoms on the surface of Cu nanoclusters. Because of their high surface activity, the carbon/Cu nanoclusters yielded carbon/Cu nanoagglomerates via collisions. Finally, while the Cu atoms within the carbon/Cu nanoagglomerates coalesced into Cu

nanocores, the carbon atoms diffused out from the nanoagglomerates to develop the MLG. These formation processes were based on the fact that both Cu and carbon atoms have fast interdiffusion rates at a high-temperature CVD reaction and, more importantly, the solubility of carbon in Cu is very low. Although the reports have demonstrated that MLG-CuNPs possess outstanding oxidation resistivity, the harsh synthetic

temperature of the as-synthesized MLG-CuNPs have restricted them from the applications in flexible electronic devices for the next-generation portable display industry. Luechinger et al.¹⁵ prepared a powder of MLG-CuNPs by reducing flame synthesis, where the water-based copper nanocolloids were successfully printed onto a polymer substrate to form a pattern electrode with low electrical conductivity of $\sim 1.5 \text{ S cm}^{-1}$. However, the above-mentioned polymer/carbon encapsulated CuNP electrodes were generally fabricated through a multistep process, such as synthesizing target materials, inkjet printing to form the films on substrates, and sintering to minimize the resistivity of electrodes. Consequently, how to develop a facile one-step method of preparing the antioxidation electrodes of MLG-CuNPs on flexible substrates is highly demanded.

Herein, we report an expeditious chemical vapor deposition (CVD) method (Figure 1 and Section S1 of the Supporting Information) to synthesize MLG-CuNPs by wrapping MLG shells over the Cu nanocores on various substrates (e.g., polyimide film (PI), carbon cloth (CC), or Si wafer (Si)). The advantages of the presented CVD method are thoroughly discussed in Section S1.1 of the Supporting Information. Though the vaporized CuNPs could simultaneously act as a catalyst to facilitate the growth of MLG shells on CuNPs in the high-temperature CVD reaction, the as-grown gaseous MLG-CuNPs flew downstream along the CVD tube to finally deposit on substrates in a low-temperature ($\sim 230 \text{ }^\circ\text{C}$) region. The as-synthesized MLG-CuNPs are highly resistant to oxidation after being exposed to a harsh ambient annealing at $150 \text{ }^\circ\text{C}$ for 3 h and exhibited an excellent mechanical durability through a bending test. For device applications, we demonstrated that MLG-CuNPs/PI can be used as the source-drain electrodes for a flexible graphene-based field-effect transistor (G-FET) device (Section S3 of the Supporting Information). In addition, we found that MLG-CuNPs/CC shows high electrocatalytic activity toward HER in water splitting. More importantly, this MLG-CuNPs/CC electrode possesses an exceptional durability against a harsh alkaline aqueous environment during a long-term electrolysis test.

Figure 2a,b shows the SEM images of closely packed MLG-CuNPs on the Si and PI substrates, respectively, where the size of quasi-circular MLG-CuNPs was calculated to be $52 \pm 9 \text{ nm}$ (Figure S3) from the TEM image (like Figure 2c). The elemental compositions of the MLG-CuNPs were examined by EDX (Figure S4). The crystal structure of CuNPs was analyzed by selected area electron diffraction (SAED, the inset of Figure 2c) to be face-centered cubic (FCC) with four fringes, corresponding to the (111), (200), (220), and (311) crystal planes; notably, no fringes of copper oxides were observed. For further structural characterization, a $\sim 3 \text{ nm}$ -thick MLG shell surrounding the Cu nanocore was observed from the HR-TEM image of a MLG-CuNP (Figure 2d), where the lattice spacings of 2.1 and 3.5 \AA consist well with the interplanar separations of Cu(111) and MLG, respectively.¹⁸

Raman scattering spectroscopy was employed to investigate the MLG shells on CuNPs as shown in Figure 3a, containing three well-recognized D, G, and 2D bands at 1360, 1590, and 2690 cm^{-1} , respectively. The D band reflects the disordered sp^2 carbon in graphene, the G band is due to the in-plane C–C stretching,¹⁹ and the 2D peak is caused by the double-resonant Raman scattering by two-phonon emission. The intensity ratios of the 2D to G bands (I_{2D}/I_G) and the D to G bands (I_D/I_G) were measured to be ~ 0.35 and ~ 2.04 , respectively, suggesting that the MLG shell is multilayer and possesses finite crystal

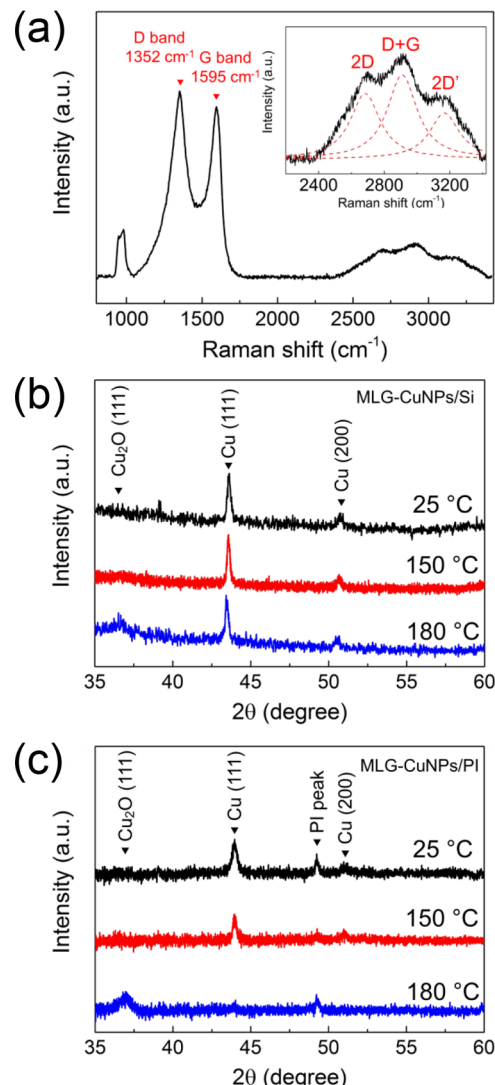


Figure 3. (a) Raman spectrum of the MLG shell after removing the Cu nanocores from MLG-CuNPs. The inset shows the deconvoluted components of the 2D, D + G, and 2D' bands. The XRD spectra of (b) MGL-CuNPs/Si and (c) MGL-CuNPs/PI in a pristine condition ($25 \text{ }^\circ\text{C}$) and after an ambient annealing for 3 h at 150 and $180 \text{ }^\circ\text{C}$, respectively.

sizes and/or plentiful edges of graphene layers. The broad bands at $2400\text{--}3400 \text{ cm}^{-1}$, deconvoluted in the inset of Figure 3a, comprise the 2D (2683 cm^{-1}), D + G (2909 cm^{-1}), and 2D' (3166 cm^{-1}) bands, wherein a nonplanar graphitic structure caused by the strain-induced effect is responsible for the D + G and 2D' bands.¹⁷ Note that this defective structure also benefits the electrocatalytic activity²⁰ toward HER, as will be discussed later.

The thermal stabilities of MLG-CuNPs/Si and MLG-CuNPs/PI were tested by ambient annealing at $\leq 180 \text{ }^\circ\text{C}$ for 3 h. Figure 3b,c shows the XRD spectra of both samples in the pristine condition (at $25 \text{ }^\circ\text{C}$) and after annealing at 150 and $180 \text{ }^\circ\text{C}$. The XRD peaks observed at $2\theta = 43.7^\circ$ and 50.6° are attributed to Cu(111) and Cu(200), respectively. It is interesting that no XRD peaks of copper oxides at $2\theta \sim 35^\circ\text{--}37^\circ$ were observed after ambient annealing of MLG-CuNPs at $150 \text{ }^\circ\text{C}$ for 3 h, suggesting that the Cu nanocore was protected efficiently by the MLG shell from oxidation. However, when MLG-CuNPs were annealed at $180 \text{ }^\circ\text{C}$ for 3

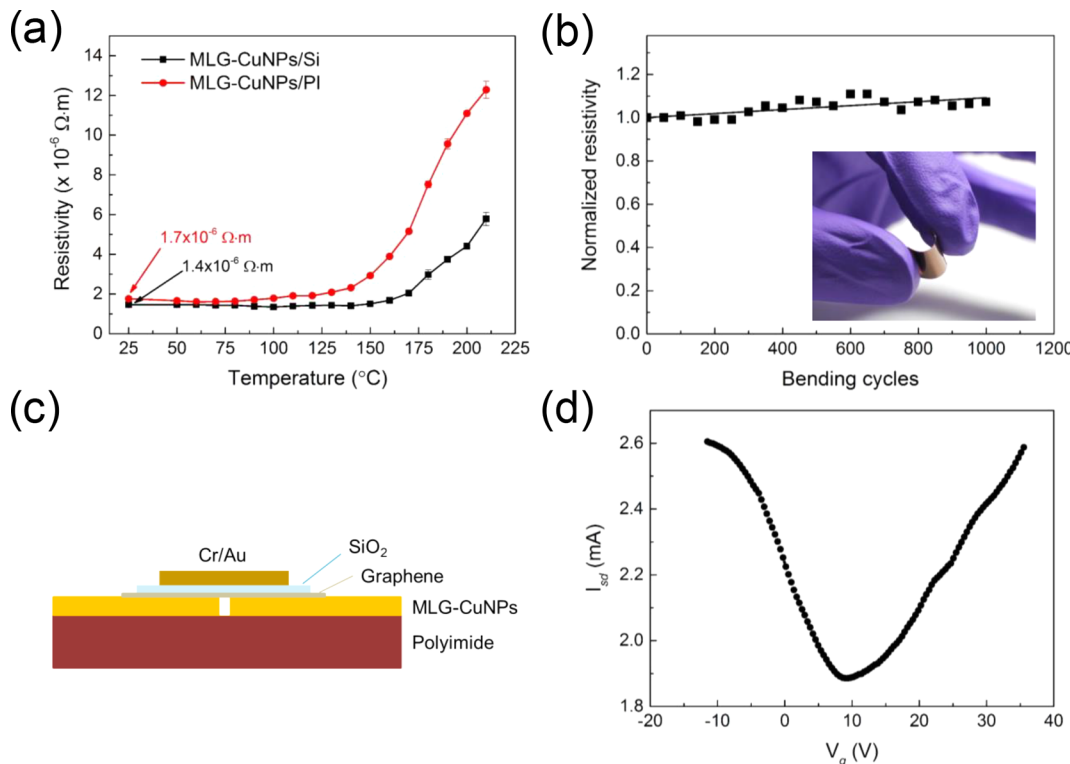


Figure 4. (a) *In situ* temperature-dependent measurements of MLG-CuNPs/Si (black curve) and MLG-CuNPs/PI (red curve) were conducted with a four-probe contact. Every presented data point was collected from the average of six measurements, where the standard deviation of the measured resistivity is less than 5% in the whole temperature range of 50–220 °C. (b) Test of the mechanical durability of the MLG-CuNPs/PI electrode was conducted by measuring the electrical resistivity after bending the electrode with a radius of curvature of 1.7 mm for 1000 cycles. The inset shows the digital image of a bendable MLG-CuNPs/PI electrode. (c) Schematic illustration of a G-FET, where MLG-CuNPs are used to fabricate the source-drain electrodes. (d) Transfer curve of the as-fabricated G-FET was obtained from the source-drain current (I_{sd}) vs gate voltage (V_g) measurement at room temperature with a bias voltage of 100 mV.

h, the Cu nanocore oxidized and a weak peak of $\text{Cu}_2\text{O}(111)$ at $2\theta = 36.6^{\circ}$ appeared. Copper oxides could grow at the grain boundaries of the MLG because of the existence of structural defects on the highly curved MLG shell. These XRD investigations indicate that both MLG-CuNPs/Si and MLG-CuNPs/PI sustain their antioxidation abilities in the 3 h annealing up to 150 °C. The higher crystallinity of MLG-CuNPs/Si than those of MLG-CuNPs/PI is observed due to the smoother surface of the Si substrate²¹ than that of a PI film (as shown in Figure S5). The complementary XPS measurements and other structural characterizations are also discussed in Section S2.

The *in situ* temperature-dependent resistivity measurements of MLG-CuNPs/Si and MLG-CuNPs/PI at 50–220 °C are displayed in Figure 4a, in which the resistivities of 1.4×10^{-6} and $1.7 \times 10^{-6} \Omega \cdot m$ for both pristine samples are ~100-fold lower than those of earlier reports.¹⁵ The resistivity of MLG-CuNPs/Si does not alter significantly in the annealing up to 150 °C, despite a slight resistivity increase in MLG-CuNPs/PI at 150 °C. These results consist with the aforementioned XRD analysis that the Cu nanocore was protected efficiently by the MLG shell from oxidation at ≤ 150 °C. The excellent mechanical durability of a flexible MLG-CuNPs/PI was verified by ~7% only increase in resistivity for 1000 bending cycles (Figure 4b). In addition, a flexible G-FET device was fabricated on a PI substrate with a pair of MLG-CuNPs-based source-drain electrodes as illustrated schematically in Figure 4c. The electrical transport of the ambipolar G-FET was characterized by measuring the transfer curve (Figure 4d), where the

obtained mobilities of holes ($\sim 940 \text{ cm}^2 \text{ V}^{-1} \text{ s}^{-1}$) and electrons ($\sim 800 \text{ cm}^2 \text{ V}^{-1} \text{ s}^{-1}$) with a charge neutrality point at ~9 V exhibit the active charge carriers of opposite polarities in the unintentionally *p*-doped graphene channel of the as-fabricated G-FET device.

Finally, it is well-known that the use of Cu-based electrodes for the energy research on water splitting was seriously limited due to the poor stability of the Cu-based electrodes in aqueous solution,²² despite the fact that Cu is a highly conductive, earth-abundant, low-cost, and low-toxic catalyst. Nevertheless, with the protection by the MLG shell, MLG-CuNPs may survive in electrochemical reactions. To this end, we synthesized MLG-CuNPs on a flexible carbon cloth substrate (MLG-CuNPs/CC) as an electrocatalytic electrode for HER. The details of electrochemical measurements are shown in Section S4 of the Supporting Information. The application of MLG-CuNPs/CC for HER has several advantages. First, the electrically conductive and chemically stable CC substrate can provide a high surface area for loading MLG-CuNPs. Second, the nanosized CuNPs can further increase the electrocatalytic surface area and electrical conductivity. Third, while the MLG shell can serve as a protective layer with good conductivity, the structural defects on the highly curved MLG shell can beneficially act as an efficient electro-catalyst toward HER in water splitting.

Figure 5a shows the measured polarization curves of HER by employing the bare CC, MLG/CC, CuNPs/CC, and MLG-CuNPs/CC electrodes, respectively. The overpotentials required to drive $J_{\text{cathodic}} = 10 \text{ mA cm}^{-2}$ for the MLG/CC,

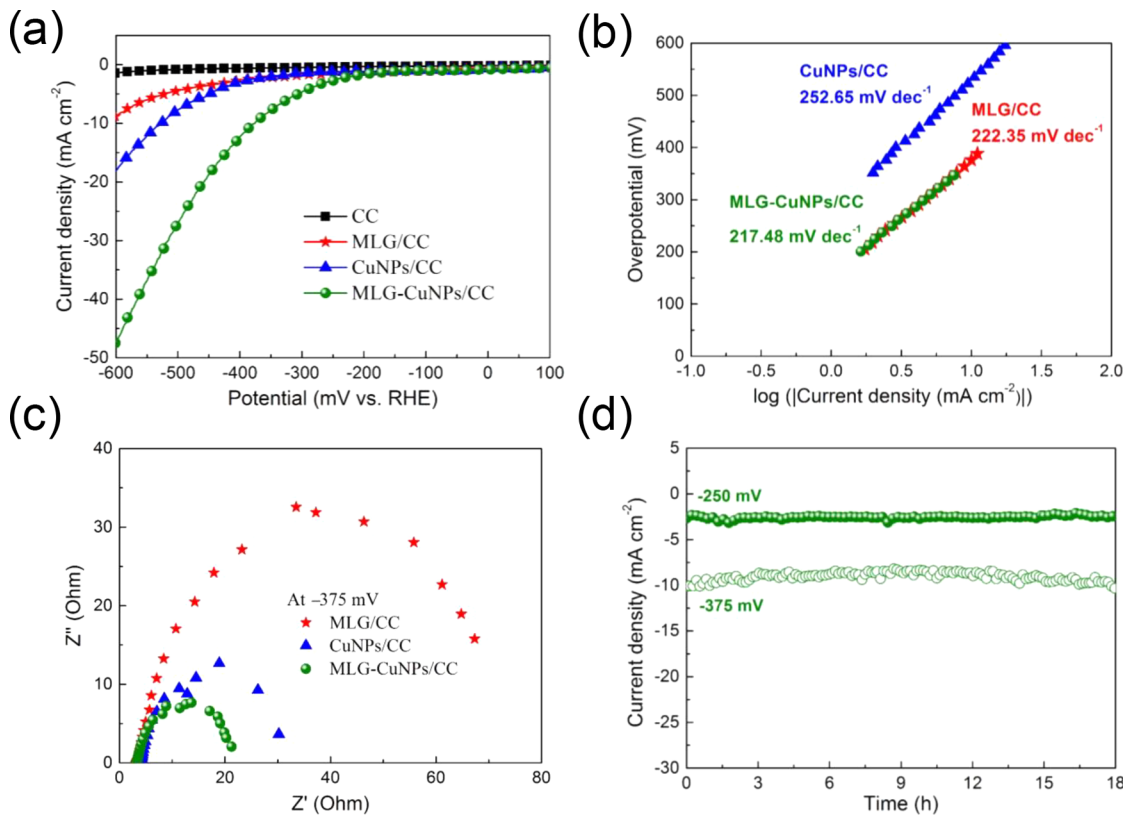


Figure 5. (a) Polarization curves of the bare CC, MLG/CC, CuNPs/CC, and MLG-CuNPs/CC electrodes were measured in N_2 -purged 1 M KOH. All data points are the original results without the iR -correction. (b) Tafel plots of the MLG/CC, CuNPs/CC, and MLG-CuNPs/CC electrodes. (c) Comparison of the Nyquist plots of the MLG/CC, CuNPs/CC, and MLG-CuNPs/CC electrodes, which were measured at an overpotential of -375 mV and scanned from 100 kHz to 10 mHz. (d) Time-dependent cathodic current densities of a MLG-CuNPs/CC electrode were tested for 18 h at the fixed overpotentials of -250 and -375 mV, respectively.

CuNPs/CC, and MLG-CuNPs/CC electrodes are -615 , -530 , and -375 mV, respectively. As compared with several earlier reports,^{23,24} the Cu-based electrocatalytic electrodes usually require the overpotential of at least -400 mV to reach $J_{\text{cathodic}} = 10 \text{ mA cm}^{-2}$. Therefore, the less required overpotential of MLG-CuNPs/CC at -375 mV demonstrates this electrode to be a more active Cu-based electro-catalyst to produce $J_{\text{cathodic}} = 10 \text{ mA cm}^{-2}$. The Tafel plots for the MLG/CC, CuNPs/CC, and MLG-CuNPs/CC electrocatalytic electrodes are displayed in Figure 5b, where the Tafel slopes of all electrodes fall in the short-range of 215 – 255 mV decade⁻¹, suggesting no dramatic difference in the intrinsic activities of the electrodes.

The Nyquist plot in Figure 5c, obtained from electrochemical impedance spectroscopy (EIS), indicates that MLG-CuNPs/CC has the smallest charge-transfer resistance (R_{ct}) among all of the tested electrodes. A lower R_{ct} value (i.e., with the smaller semicircle) in the Nyquist plot corresponds to the faster charge transfer between electrodes and electrolytes. The smallest R_{ct} of MLG-CuNPs/CC also supports the best HER performance of the MLG-CuNPs/CC electrode in the polarization curve measurements (Figure 5a). It is known that with the lower R_{ct} of MLG-CuNPs/CC, the more efficient charge transport can be achieved, which stems from the synergistic effect on the conductive counterparts between the MLG protective shells and CuNP nanocores. Namely, the MLG shells can remarkably prevent the CuNPs from oxidation (Figures 3b and 3c), thus maintaining the high conductivity of MLG-CuNPs/CC (Figure 4a). In a MLG-CuNP, the CuNP nanocore can act as a scaffold to support the MLG shell, meanwhile preventing the MLG

shell from collapse. In case the hollow MLG shells collapsed to stack to each other (Figure S11), these depressed MLG shells could greatly lose their large charge-transfer surface, resulting in the increase of R_{ct} . By the same token, without the protection of MLG shells, the easily oxidized CuNPs under a harsh environment would retard efficient charge transports, consequently increasing the R_{ct} as well. In contrast, the lower R_{ct} corresponds to the less energy-loss within a system; therefore, a less overpotential is required to drive the HER. As a result, the MLG-CuNPs/CC electrode shows the best HER performance (i.e., the lowest overpotential for achieving $J_{\text{cathodic}} = 10 \text{ mA cm}^{-2}$) and exhibits the lowest R_{ct} value among all electrodes examined. Moreover, a practical application of MLG-CuNPs/CC was also examined by a continuous electrolysis test over 18 h at the fixed potentials of -250 and -375 mV, where the J_{cathodic} values remained stable at ~ 2.5 and $\sim 10 \text{ mA cm}^{-2}$, respectively (Figure 5d). This exceptional durability in the harsh alkaline aqueous environment demonstrates that MLG-CuNPs/CC can be used as a prospective electrode for HER for a long-term operation.

In summary, we have developed a facile one-step CVD method to prepare low-resistance MLG-CuNPs electrodes on a flexible substrate without the requirement of post thermal annealing. The improved electrical resistivities of 1.7×10^{-6} and $1.4 \times 10^{-6} \Omega \cdot \text{m}$ for MLG-CuNPs/PI and MLG-CuNPs/Si are ~ 100 -fold lower than previous reports. The as-synthesized MLG-CuNPs exhibit an excellent antioxidation ability in the annealing up to 150 °C. In addition, the flexible MLG-CuNPs/PI possesses an excellent mechanical durability after 1000

bending cycles. A G-FET fabricated on a flexible PI substrate with a pair of MLG-CuNPs-based electrodes shows the hole and electron mobilities of ~ 940 and $\sim 800 \text{ cm}^2 \text{ V}^{-1} \text{ s}^{-1}$, respectively. Finally, the MLG-CuNPs/CC electrode for HER demonstrated a better performance than the electrodes with MLG or CuNPs alone. Besides, this MLG-CuNPs/CC electrode exhibits an exceptional HER durability in alkaline aqueous solution for a long-term period test. We envisage that this novel approach of preparing MLG-CuNPs electrodes on flexible substrates can serve as a simple, cost-effective method to fabricate portable devices in electronic and optoelectronic industries.

■ ASSOCIATED CONTENT

Supporting Information

The Supporting Information is available free of charge on the ACS Publications website at DOI: [10.1021/acsami.7b06490](https://doi.org/10.1021/acsami.7b06490).

CVD synthesis of MLG-CuNPs, material characterizations, MLG-CuNPs-based source-drain electrodes in a G-FET device, and MLG-CuNPs/CC as an electrocatalytic electrode in HER ([PDF](#))

■ AUTHOR INFORMATION

Corresponding Author

*Y.-T. Chen. E-mail: ytccchem@ntu.edu.tw.

ORCID

Yit-Tsong Chen: [0000-0002-6204-8320](https://orcid.org/0000-0002-6204-8320)

Notes

The authors declare no competing financial interest.

■ ACKNOWLEDGMENTS

This work was supported, in part, by the Ministry of Science and Technology (MOST) of Taiwan under Grant Nos. 105-2627-M-002-001 and 103-2113-M-002-014-MY3. We thank the assistance from Ms. Su-Jen Ji for SEM characterizations and from Mr. Hsueh-Ren Chen for TEM operations.

■ REFERENCES

- (1) Jeong, S.; Lee, S. H.; Jo, Y.; Lee, S. S.; Seo, Y.-H.; Ahn, B. W.; Kim, G.; Jang, G.-E.; Park, J.-U.; Ryu, B.-H.; Choi, Y. Air-Stable, Surface-Oxide Free Cu Nanoparticles for Highly Conductive Cu Ink and Their Application to Printed Graphene Transistors. *J. Mater. Chem. C* **2013**, *1*, 2704–2710.
- (2) Tseng, C.-A.; Han, H.-C.; Chong, C.-W.; Chang, C.-C.; Lin, C.-F.; Wang, S.-B.; Tseng, W.-H.; Wu, C.-I.; Lee, J.-H.; Chang, S.-J.; Chen, K.-H.; Chen, L.-C. The Effects of Fluorine-Contained Molecules on Improving the Polymer Solar Cell by Curing the Anomalous S-Shaped I – V Curve. *ACS Appl. Mater. Interfaces* **2015**, *7*, 6683–6689.
- (3) Xu, S.; Man, B.; Jiang, S.; Wang, J.; Wei, J.; Xu, S.; Liu, H.; Gao, S.; Liu, H.; Li, Z.; Li, H.; Qiu, H. Graphene/Cu Nanoparticle Hybrids Fabricated by Chemical Vapor Deposition As Surface-Enhanced Raman Scattering Substrate for Label-Free Detection of Adenosine. *ACS Appl. Mater. Interfaces* **2015**, *7*, 10977–10987.
- (4) Xu, S.; Jiang, S.; Wang, J.; Wei, J.; Yue, W.; Ma, Y. Graphene Isolated Au Nanoparticle Arrays with High Reproducibility for High-Performance Surface-Enhanced Raman Scattering. *Sens. Actuators, B* **2016**, *222*, 1175–1183.
- (5) Berglund, S. P.; He, H.; Chemelewski, W. D.; Celio, H.; Dolocan, A.; Mullins, C. B.P-Si/W2C and P-Si/W2C/Pt Photocathodes for the Hydrogen Evolution Reaction. *J. Am. Chem. Soc.* **2014**, *136*, 1535–1544.
- (6) Sanchez-Romaguera, V.; Wünscher, S.; Turki, B. M.; Abbel, R.; Barbosa, S.; Tate, D. J.; Oyeka, D.; Batchelor, J. C.; Parker, E. a.; Schubert, U. S.; Yeates, S. G. Inkjet Printed Paper Based Frequency Selective Surfaces and Skin Mounted RFID Tags: The Interrelation between Silver Nanoparticle Ink, Paper Substrate and Low Temperature Sintering Technique. *J. Mater. Chem. C* **2015**, *3*, 2132–2140.
- (7) Magdassi, S.; Grouchko, M.; Kamyshny, A. Copper Nanoparticles for Printed Electronics: Routes Towards Achieving Oxidation Stability. *Materials* **2010**, *3*, 4626–4638.
- (8) Xu, S.; Zhan, J.; Man, B.; Jiang, S.; Yue, W.; Gao, S.; Guo, C.; Liu, H.; Li, Z.; Wang, J.; Zhou, Y. Real-Time Reliable Determination of Binding Kinetics of DNA Hybridization Using a Multi-Channel Graphene Biosensor. *Nat. Commun.* **2017**, *8*, 14902.
- (9) Xu, S.; Man, B.; Jiang, S.; Yue, W.; Yang, C.; Liu, M.; Chen, C.; Zhang, C. Direct Growth of Graphene on Quartz Substrates for Label-Free Detection of Adenosine Triphosphate. *Nanotechnology* **2014**, *25*, 165702.
- (10) Liao, C.-D.; Lu, Y.-Y.; Tamalampudi, S. R.; Cheng, H.-C.; Chen, Y.-T. Chemical Vapor Deposition Synthesis and Raman Spectroscopic Characterization of Large-Area Graphene Sheets. *J. Phys. Chem. A* **2013**, *117*, 9454–9461.
- (11) Chen, C. C.; Kuo, C. J.; Liao, C. D.; Chang, C. F.; Tseng, C. A.; Liu, C. R.; Chen, Y. T. Growth of Large-Area Graphene Single Crystals in Confined Reaction Space with Diffusion-Driven Chemical Vapor Deposition. *Chem. Mater.* **2015**, *27*, 6249–6258.
- (12) Schriver, M.; Regan, W.; Gannett, W. J.; Zaniewski, A. M.; Crommie, M. F.; Zettl, A. Graphene as a Long-Term Metal Oxidation Barrier: Worse than Nothing. *ACS Nano* **2013**, *7*, 5763–5768.
- (13) Zhu, J.; Yang, D.; Yin, Z.; Yan, Q.; Zhang, H. Graphene and Graphene-Based Materials for Energy Storage Applications. *Small* **2014**, *10*, 3480–3498.
- (14) Stankovich, S.; Dikin, D. a.; Domke, G. H. B.; Kohlhaas, K. M.; Zimney, E. J.; Stach, E. a.; Piner, R. D.; Nguyen, S. T.; Ruoff, R. S. Graphene-Based Composite Materials. *Nature* **2006**, *442*, 282–286.
- (15) Luechinger, N. A.; Athanassiou, E. K.; Stark, W. J. Graphene-Stabilized Copper Nanoparticles as an Air-Stable Substitute for Silver and Gold in Low-Cost Ink-Jet Printable Electronics. *Nanotechnology* **2008**, *19*, 445201.
- (16) Lee, S.; Hong, J.; Koo, J. H.; Lee, H.; Lee, S.; Choi, T.; Jung, H.; Koo, B.; Park, J.; Kim, H.; Kim, Y.-W.; Lee, T. Synthesis of Few-Layered Graphene Nanoballs with Copper Cores Using Solid Carbon Source. *ACS Appl. Mater. Interfaces* **2013**, *5*, 2432–2437.
- (17) Wang, S.; Huang, X.; He, Y.; Huang, H.; Wu, Y.; Hou, L.; Liu, X.; Yang, T.; Zou, J.; Huang, B. Synthesis, Growth Mechanism and Thermal Stability of Copper Nanoparticles Encapsulated by Multi-Layer Graphene. *Carbon* **2012**, *50*, 2119–2125.
- (18) Ishigami, M.; Chen, J. H.; Cullen, W. G.; Fuhrer, M. S.; Williams, E. D. Atomic Structure of Graphene on SiO₂. *Nano Lett.* **2007**, *7*, 1643–1648.
- (19) Pimenta, M. a.; Dresselhaus, G.; Dresselhaus, M. S.; Cançado, L. G.; Jorio, A.; Saito, R. Studying Disorder in Graphite-Based Systems by Raman Spectroscopy. *Phys. Chem. Chem. Phys.* **2007**, *9*, 1276–1291.
- (20) Punckt, C.; Pope, M. A.; Liu, J.; Lin, Y.; Aksay, I. A. Electrochemical Performance of Graphene as Effectuated by Electrode Porosity and Graphene Functionalization. *Electroanalysis* **2010**, *22*, 2834–2841.
- (21) Lee, J.; Kwak, S. H.; Kim, H. J. Effects of Substrates Roughness on c-Axis Preferred Orientation of ZnO Films Deposited by RF Magnetron Sputtering. *Thin Solid Films* **2003**, *423*, 262–266.
- (22) Paracchino, A.; Mathews, N.; Hisatomi, T.; Stefk, M.; Tilley, S. D.; Grätzel, M. Ultrathin Films on Copper(i) Oxide Water Splitting Photocathodes: A Study on Performance and Stability. *Energy Environ. Sci.* **2012**, *5*, 8673.
- (23) Du, J.; Wang, J.; Ji, L.; Xu, X.; Chen, Z. A Highly Active and Robust Copper-Based Electrocatalyst toward Hydrogen Evolution Reaction with Low Overpotential in Neutral Solution. *ACS Appl. Mater. Interfaces* **2016**, *8*, 30205–30211.
- (24) Kumar, B.; Saha, S.; Basu, M.; Ganguli, A. K. Enhanced Hydrogen/oxygen Evolution and Stability of Nanocrystalline (4–6 nm) Copper Particles. *J. Mater. Chem. A* **2013**, *1*, 4728–4735.

Supporting Information

One-step synthesis of anti-oxidative graphene-wrapped copper nanoparticles on flexible substrates for electronic and electro-catalytic applications

Chi-Ang Tseng,[†] Chiao-Chen Chen,[†] Rajesh Kumar Ulaganathan,[†] Chuan-Pei Lee,[†] Hsu-Cheng Chiang,[†] Chin-Fu Chang,[†] and Yit-Tsong Chen^{†,§,}*

[†] Department of Chemistry, National Taiwan University, No. 1, Sec. 4, Roosevelt Road, Taipei 106, Taiwan

[§] Institute of Atomic and Molecular Sciences, Academia Sinica, P.O. Box 23-166, Taipei 106, Taiwan

^{*}*Address correspondence to: ytccchem@ntu.edu.tw*

S1. CVD synthesis of MLG-CuNPs

Figure 1 (in the main text) illustrates the experimental setup for the synthesis of vapor-phase MLG-CuNPs in CVD reaction with the self-assisted catalytic growth of the MLG shell on CuNPs. The CVD system is composed of a temperature-programmable furnace (40 cm in length) and a quartz tube of 1 inch in diameter. The temperature profile along the quartz tube for the growth of MLG-CuNPs at 1090 °C is displayed in Figure S1. One end of the reaction tube is a gas inlet and the other end was evacuated with a dry pump or a diffusion/mechanical pumping system. The gaseous precursors used in the synthetic reaction of MLG-CuNPs were methane (CH₄, FMI gas Co. Ltd., 99.9995 %) and hydrogen (H₂, FMI gas Co. Ltd., 99.9995 %) with the flow rates of 200 sccm CH₄ and 20 sccm H₂ in the CVD reaction. The collector substrates of Si wafer (with a 300 nm-thick SiO₂ dielectric layer), PI film (100 μm in thickness), or carbon cloth (CC, W0S1002, 360 μm in thickness, the sheet resistance of 0.63 Ω sq⁻¹) were put inside the quartz tube and located ~3 cm away from the furnace edge. After setting the collector substrates, a 25 μm-thick Cu foil (Alfa Aesar, purity 99.8 %) was mounted on a tungsten boat, placed inside the quartz tube, and located at the center of the furnace. The separation distance between the Cu foil and collector substrates is ~20 cm. The furnace was then heated to 1090 °C at a rising rate of 25 °C min⁻¹. Before reaction, an Ar gas flow at 50 sccm was used to clean up the reaction tube for 30 min. During the synthetic reaction of MLG-CuNPs, the as-synthesized CuNPs could simultaneously self-assist the catalytic formation of MLG shells on CuNPs. Finally, the as-grown vapor-phase MLG-CuNPs were carried by the gas flow to deposit onto the collector substrates for 2 hours, where the deposition temperature was maintained at ~230 °C (Figure S1).

For comparison in the water-splitting experiments, the CuNPs/CC sample was synthesized with the same synthetic protocols as described above, except without introducing the precursors of CH₄ and H₂. The MLG/CC sample was obtained by immersing the as-synthesized MLG-CuNPs/CC in HNO₃ solution to dissolve/eliminate the Cu nanocores.

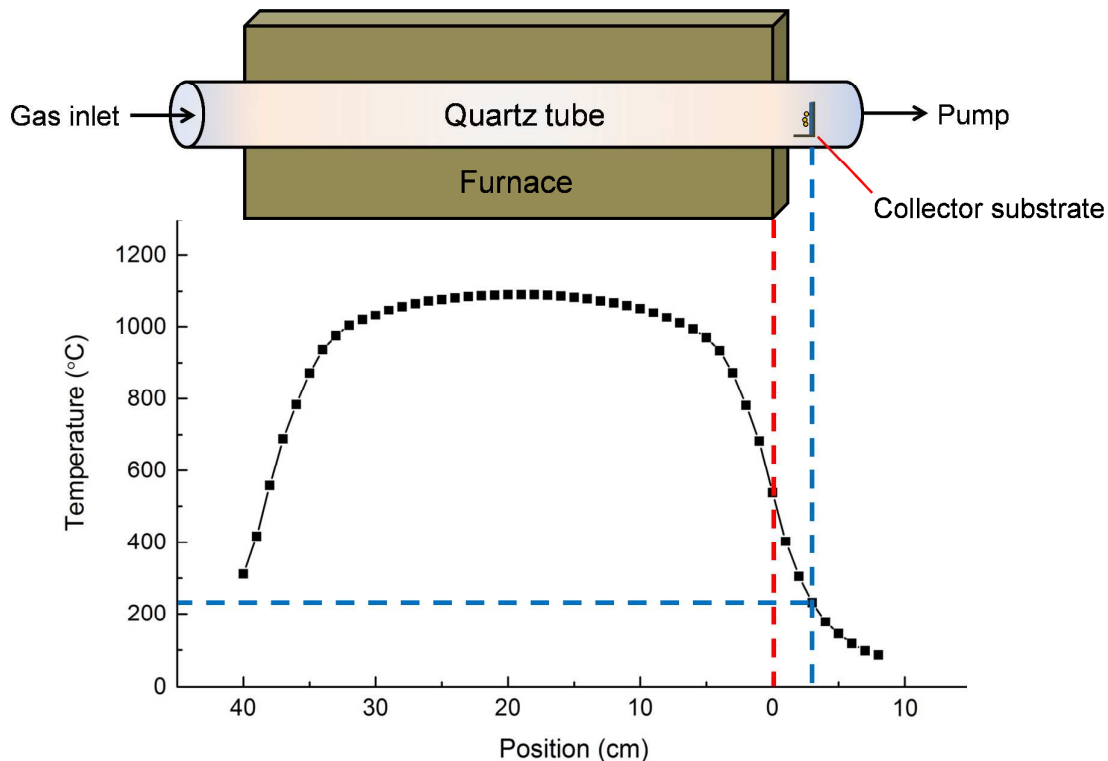


Figure S1. The temperature profile inside the quartz tube of a CVD system was measured with a K-type thermocouple equipped with a thermometer (Hila Co. Ltd., CHY-502), where the reaction temperature was set at 1090 °C. The collector substrate inside the quartz tube is ~3 cm away from the furnace edge; the deposition temperature at the collector substrate is ~230 °C.

S1.1. Advantages of presented CVD method

In the CVD synthesis of vapor-phase MLG-CuNPs, the self-assisted catalytic growth of the MLG shell on CuNPs provides three advantages. First, the formation of MLG-CuNPs would be impossible by directly taking CuNPs and CH₄ as reaction precursors, because the

CuNPs with relatively low melting point (~ 900 °C)^{S1} could not stand the high-temperature reaction of synthesizing/annealing the MLG shells at >1000 °C. In contrast, the vapor-phase CuNPs, formed from the vaporization of Cu foils in our method, could not only self-assist the growth of the MLG shell on CuNPs, but also escape from the agglomeration of MLG-CuNPs during the high-temperature synthesis. Secondly, this vapor-phase synthesis method is suitable for the growth of MLG-CuNPs on a flexible substrate (e.g., a PI film), which could not endure the MLG synthesis reaction at >1000 °C. It is noted that the fabrication of portable devices on flexible substrates is highly demanded for the next-generation electronic and optoelectronic industries. Despite several earlier reports of synthesizing graphene on Cu substrates at 600–750 °C,^{S2–S4} these thermal conditions at >600 °C are still a challenge to grow graphene on a flexible substrate. Comparatively, with our experimental design, the collector substrates in the CVD reaction were located in an effective annealing, but relatively low-temperature, region at ~ 230 °C (as shown in Figures 1 and S1), which is also in accordance with the post-treatment (thermal annealing) temperature in several previous reports.^{S5,S6} Thirdly, a post thermal annealing process is generally required for the polymer/carbon-encapsulated CuNPs electrodes with an ink-jet printing method to enhance the electrical conductivity; in stark contrast, the post thermal annealing is unnecessary in our approach, because the MLG-CuNPs were *in situ* annealed during the CVD reaction. To prove this effective *in situ* annealing of MLG-CuNPs in our experiments, we demonstrated in Figure S2 the negligible variation of the resistivity of the as-prepared MLG-CuNPs with the post annealing treatments at 150–300 °C.

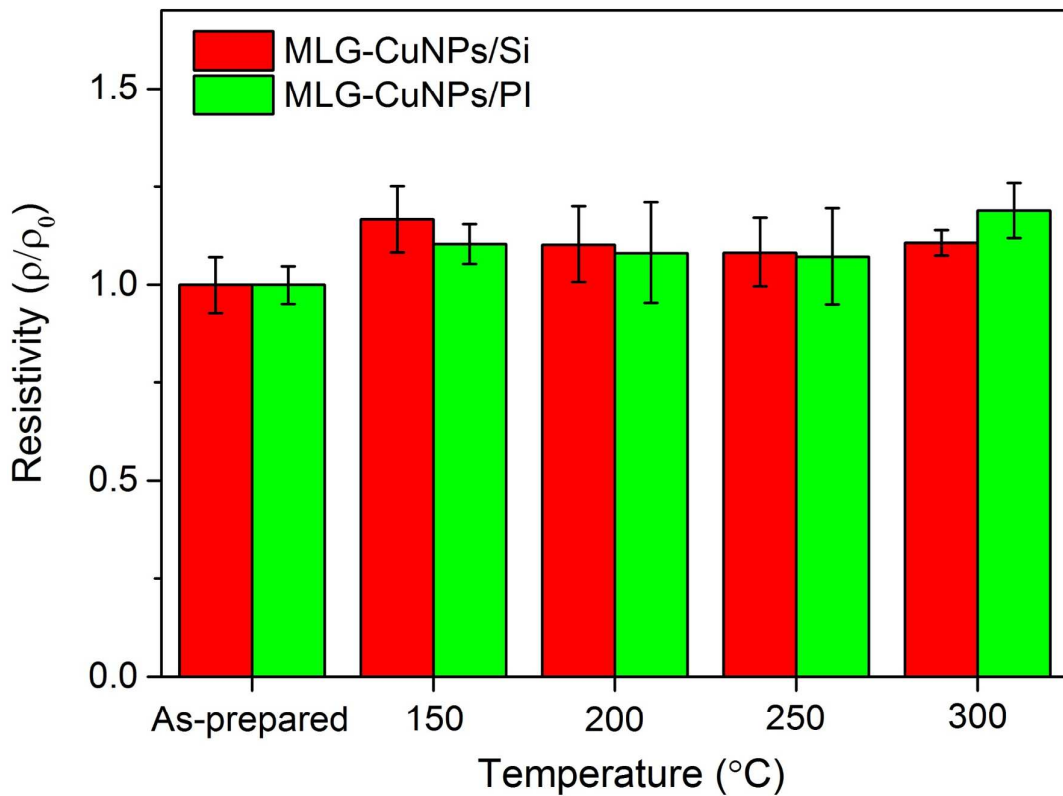


Figure S2. The resistivities of MLG-CuNPs/Si and MLG-CuNPs/PI were measured in the post annealing tests at different temperatures. No significant changes in the resistivities of MLG-CuNPs/Si and MLG-CuNPs/PI were observed in the post thermal annealing up to 300 °C, indicating the *in situ* annealing is effective during the synthetic process and a post annealing is unnecessary. The resistivity presented at each temperature is the average from five measurements.

S2. Material characterizations

The morphology and size of the as-grown MLG-CuNPs were observed by field-emission scanning electron microscopy (FESEM) (JEOL, JSM 7600) with an accelerating voltage of 10 kV and by transmission electron microscopy (TEM) (Hitachi, H-7100) with an accelerating voltage of 200 kV. High-resolution transmission electron microscopy (HRTEM) (Philips Tecnai F30) equipped with an energy dispersive X-ray (EDX) spectrometer operated at an accelerating voltage of 300 kV was employed to examine the elemental compositions of MLG-CuNPs and the lattice spacing of the MLG shell. A TEM grid of nickel mesh with carbon-film coating was used to deposit MLG-CuNPs for TEM imaging. An X-ray diffraction (XRD) (X’Pert PRO-PANalytical, Cu K α 1 radiation at $\lambda = 1.54 \text{ \AA}$) analysis at the scan range of 30°–60° was used to characterize the oxidation state of the Cu nanocore in MLG-CuNPs. X-ray photoelectron spectroscopy (XPS) with an anode X-ray gun of 15 kV (VG Scientific ESCALAB 250) was applied to verify the surface compositions of MLG-CuNPs. Raman scattering spectra of the MLG shells were recorded in a confocal Raman microscope (NT-MDT, NTMDT NTEGRA Spectra) using a 488 nm laser as an excitation source. Surface topograph and surface roughness of different growth substrates (i.e., a Si wafer or a PI film) were scanned by atomic force microscopy (AFM) (Digital Instruments, Bioscope SZ). The AFM measurements were conducted by area-scans ($20 \times 20 \mu\text{m}^2$) on different spots in tapping mode with 256 scan lines and 256 line samples. *In situ* temperature-dependent electrical resistance of MLG-CuNPs in the range of 50–220 °C was measured with a Keithley Series 2000 Digital Multimeter. The mechanical durability of a MLG-CuNPs/PI was investigated using a home-made bending-test system, where one side of the MLG-CuNPs/PI was fixed on a stainless steel stage and the other side was mounted to a movable stage. The bending radius of the MLG-CuNPs/PI can be controlled by the distance between the two stages.

S2.1. Size distribution of the as-synthesized MLG-CuNPs

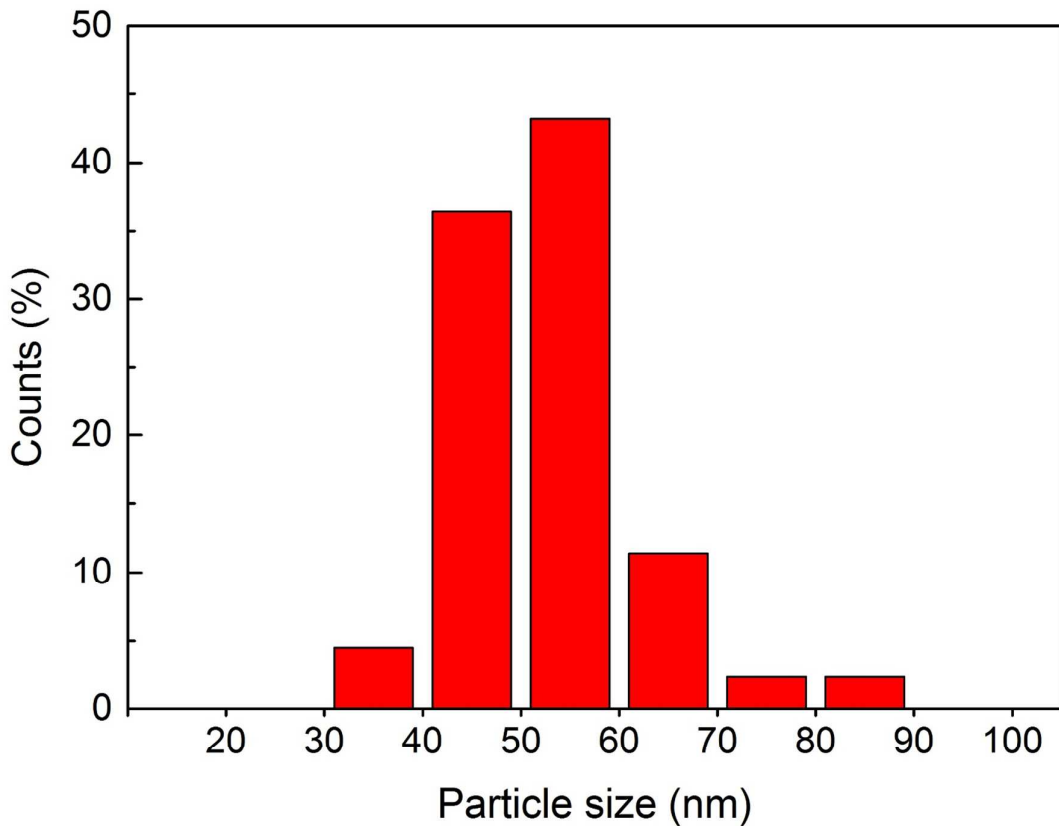


Figure S3. The size distribution of the as-synthesized MLG-CuNPs is obtained from the TEM image (like Figure 2c) and was calculated via the Nano measurer software. The average particle size of MLG-CuNPs is 52 ± 9.1 nm.

S2.2. Element compositions of the as-synthesized MLG-CuNPs

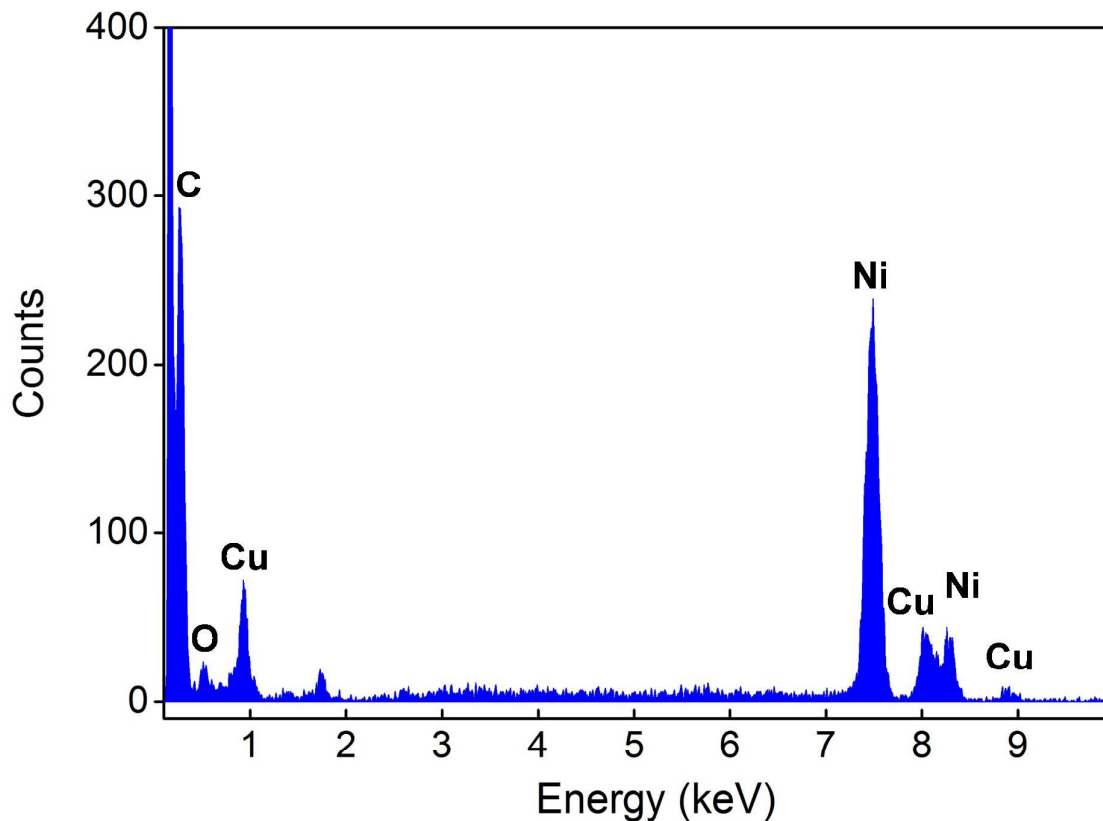


Figure S4. EDX spectroscopy was employed to examine the element compositions of the as-synthesized MLG-CuNPs, in which both the Ni peak and part of the C signal are contributed from the TEM grid of nickel mesh with carbon-film coating used in the EDX measurement.

S2.3. Surface topograph and roughness on a growth substrate

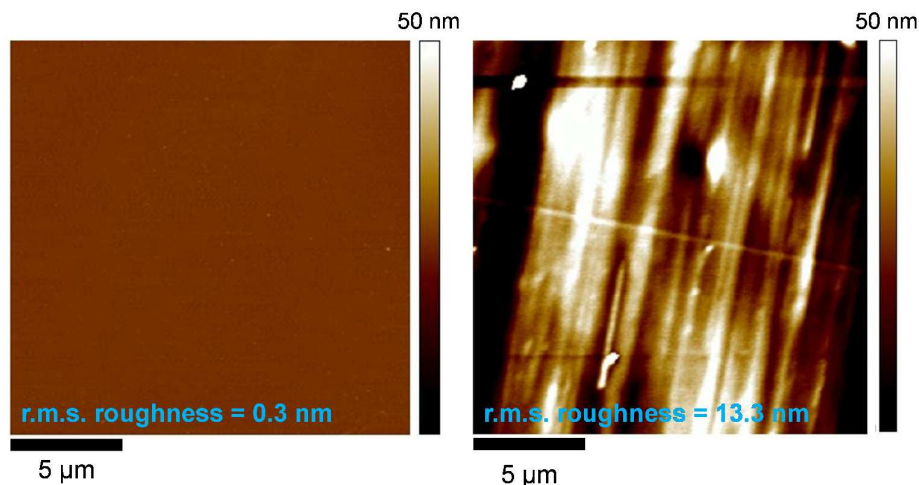


Figure S5. The surface topographs of a Si wafer (left) and a PI film (right) were scanned by AFM with tapping mode. The root-mean-squares (r.m.s.) of the average roughness on the Si wafer (left) and PI film (right) were measured to be 0.3 and 13.3 nm, respectively.

S2.4. Thickness of a MLG-CuNP electrode on a Si wafer or a PI film

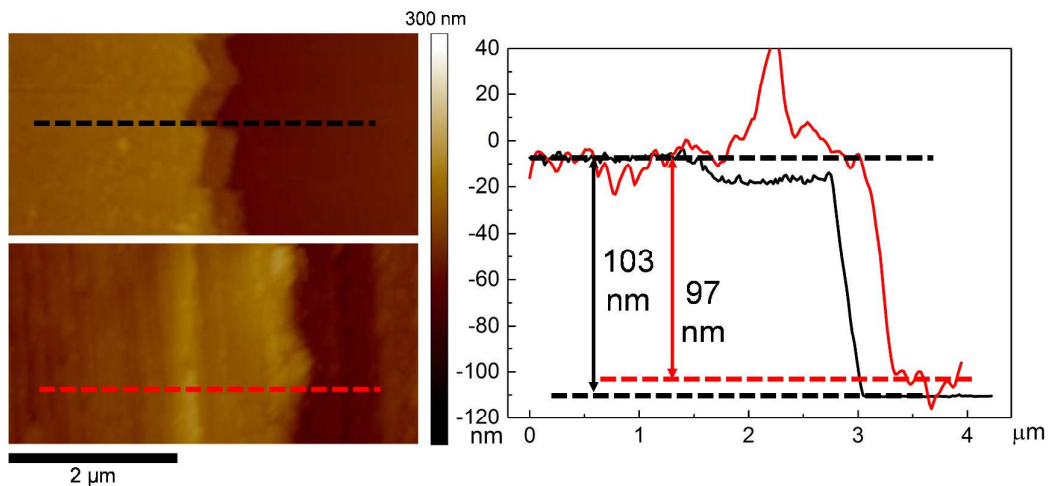


Figure S6. (left) The AFM image of a MLG-CuNP electrode on a Si wafer (top) or a PI film (bottom). (right) The section profiles across the black and red dashed-lines marked in the left panels. The thickness of the MLG-CuNP electrode was measured to be ~100 nm on either substrate.

S2.5. HR-TEM image of the MLG shell

The MLG shells were obtained by removing the Cu nanocores from MLG-CuNPs using a Marble's reagent. The left panel of Figure S7 shows a HR-TEM image of the MLG shells, in which some of the MLG shells were distorted or broken during the sample preparation. The right panel of Figure S7 displays the detailed structure of a MLG shell, which comprises about 8–10 graphene layers with the lattice spacing of ~ 3.5 Å consistent with the interplanar separation of graphitic layers.

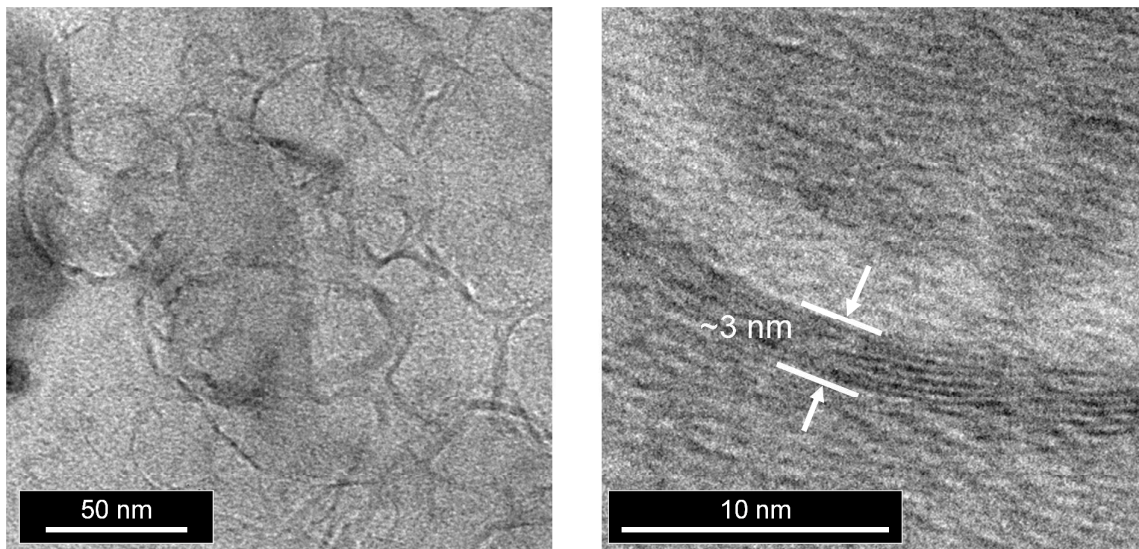


Figure S7. The HR-TEM images of MLG shells were taken after removing the Cu nanocores from MLG-CuNPs.

S2.6. Analysis of the oxidation states of Cu from the measured XPS spectra

Supplementary to the XRD analysis, which lacks of definite information about the thin copper-oxide layer formed on the CuNP surface, XPS was applied to semi-quantify the chemical compositions and their oxidation states of the CuNP surface in MLG-CuNPs. As shown in Figures S6a–b, the spectra of the Cu 2p_{3/2} cores of both MLG-CuNPs/Si and MLG-CuNPs/PI were obtained in the pristine and ambient annealing (at 150 and 180 °C) conditions. Although the XPS peak of both oxidative Cu(I) and metallic Cu(0) overlap at 932.6 eV and cannot be distinguished, the signals of the oxidative Cu(II) are well separated at 933.8 eV and 940–945 eV. As shown in Figures S6a–b, the XPS spectra of both MLG-CuNPs/Si and MLG-CuNPs/PI in the pristine condition (i.e., at 25 °C) are free of the oxidative Cu(II) peaks. A detailed analysis reveals that after a 150 °C annealing, the MLG-CuNPs/Si (or MLG-CuNPs/PI) already contained 69 % (or 90 %) of Cu(II) on the CuNP surface as listed in Table S1. With an even higher-temperature treatment at 180 °C, the CuNP surface was oxidized completely to ~100 % of Cu(II). These XPS results indicate the growth of a very thin CuO layer on the CuNP surface after annealing, which will consequently degrade the electrical conduction among MLG-CuNPs (cf. Figure 4a).

The oxidation of the MLG shell in the annealing has also been examined by XPS. Figure S6c shows the XPS spectra of the C 1s core in MLG-CuNPs/Si before and after 180 °C annealing for 3 hours. Before annealing, the signal could be deconvoluted into sp² (C=C) at 284.3 eV and sp³ (C–C) at 285.3 eV. After annealing, while the original peaks of both sp² (C=C) and sp³ (C–C) still existed, a new additional peak belonging to the carbonyl group (C=O) at 288.0 eV appeared. This outcome indicates that the highly curved MLG shell on the Cu nanocore was defective and subjected to easy oxidation during the annealing. As a result, ambient oxygen could oxidize the defective MLG shell and/or penetrate into the Cu nanocore to induce an oxidative reaction.

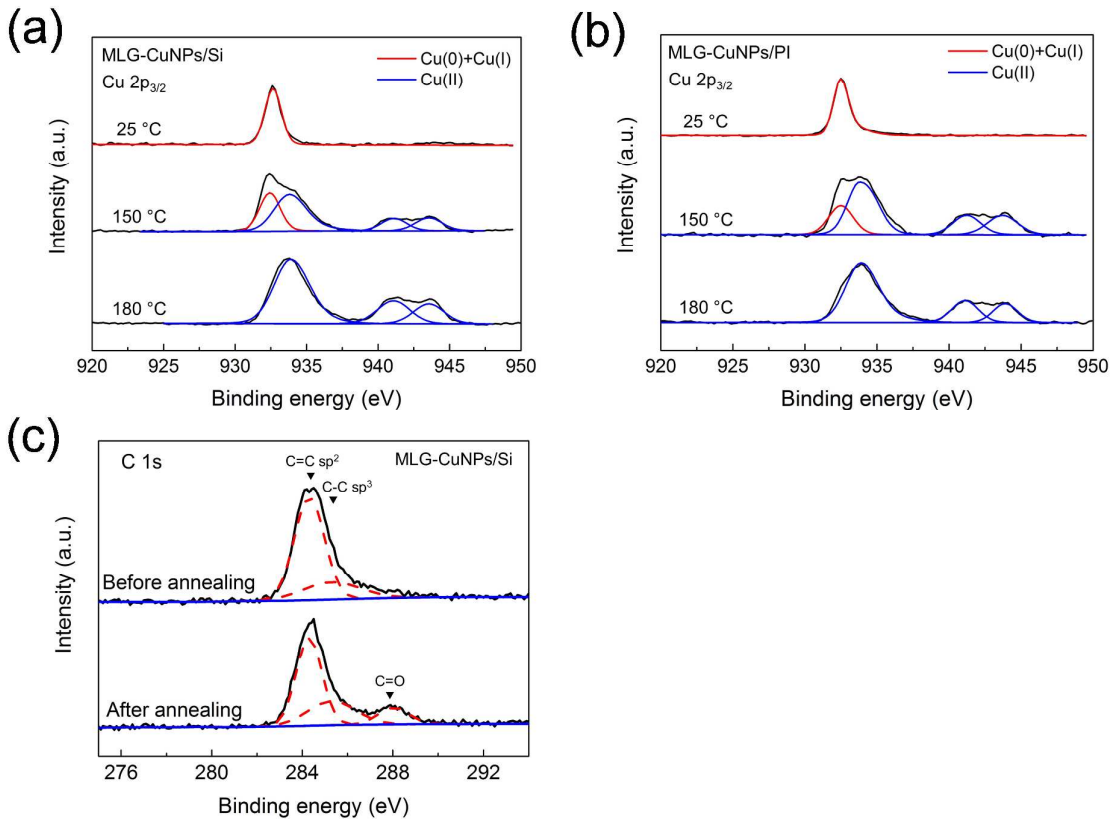


Figure S8. XPS spectra of the Cu 2p_{3/2} core for (a) MLG-CuNPs/Si and (b) MLG-CuNPs/PI were investigated in a pristine condition (25 °C) and after the ambient annealing treatments at 150 and 180 °C for 3 hours. A Gaussian (10%)-Lorentzian (90%) peak-shape was used to deconvolute the Cu 2p_{3/2} peaks. The contents of both Cu(0)+Cu(I) and Cu(II) in each sample were calculated and are listed in Table S1. (c) XPS spectra of the C 1s core of the MLG-CuNPs/Si before and after a 3-hour annealing at 180 °C. It is also noted that due to the inelastic mean-free-path of the emission electrons from Cu, only the emission electrons in the ~1 nm-thick outmost surface can be extracted as XPS signals.^{S7}

The oxidation condition of the CuNP surface was further investigated by spectroscopically deconvoluting the observed Cu 2p_{3/2} peaks. According to Biesinger et al.,^{S8} the contents of both Cu(0)+Cu(I) and Cu(II) states can be calculated by

$$\text{Cu(0)+Cu(I)} (\%) = \frac{A \times (A_{1s}/B_s)B}{A+B} \times 100 \quad \text{and} \quad \text{Cu(II)} (\%) = \frac{B \times (1+(A_{1s}/B_s))}{A+B} \times 100,$$

where A and B represent the areas of the main peak (including both Cu(II) and Cu(0)+Cu(I) signals) and the shake-up peak (only the Cu(II) signal), respectively. The A_{1s}/B_s is the

intensity ratio of the main peak to the satellite peak of CuO in a standard sample. An analysis from the observed spectra of Figures S6a–b gives the contents of both Cu(0)+Cu(I) and Cu(II) states, which are summarized in Table S1.

Table S1. The contents of both Cu(0)+Cu(I) and Cu(II) states in the MLG-CuNPs/Si and MLG-CuNPs/PI samples in the pristine condition (at 25 °C) and after the annealing treatments at 150 and 180 °C.

MLG-CuNPs/Si	Cu(0)+Cu(I)	Cu(II)	MLG-CuNPs/PI	Cu(0)+Cu(I)	Cu(II)
25 °C	100	0	25 °C	100	0
150 °C	31	69	150 °C	10	90
180 °C	0	100	180 °C	0	100

S2.7. XPS spectra of Cu nanocores, MLG-CuNPs, and MLG

The XPS spectra with a wide energy scan of 0–1200 eV for Cu nanocores, MLG-CuNPs, and MLG are shown in the left panel of Figure S9. An apparent increase of the carbon signal at ~284 eV from Cu nanocores to MLG-CuNPs or MLG is clearly seen. The very weak intensity of carbon signal exists in the spectrum of Cu nanocores is frequently found on the sample surface exposed to air due to the presence of adventitious carbons from the chemical species, such as atmospheric CO and CO₂.⁵⁹ It is also noted that the XPS spectrum of MLG contains no Cu signals at 920–950 eV, demonstrating the effective removal of Cu cores from MLG-CuNPs. The right panel of Figure S9 displays the expanded-scale XPS signal of the C 1s for MLG (taken from the left panel), which is deconvoluted into the sp² (C=C) peak at 284.3 eV and the sp³ (C–C) peak at 285.4 eV, suggesting the existence of graphene.

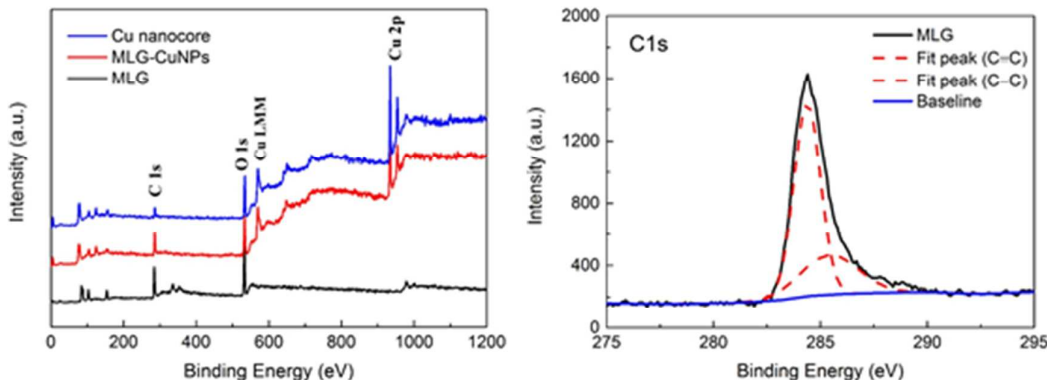


Figure S9. (left) The observed XPS spectra of Cu nanocores, MLG-CuNPs, and MLG. (right) Spectroscopic deconvolution of the C 1s signal of MLG into the sp² (C=C) peak at 284.3 eV and the sp³ (C–C) peak at 285.4 eV.

S3. MLG-CuNPs-based source-drain electrodes in a G-FET device

To fabricate a G-FET device, monolayer graphene was synthesized on a 25- μm -thick Cu foil in a low-pressure CVD reaction.^{S10} For the graphene synthesis, a Cu foil was cleaned by glacial acetic acid (Sigma-Aldrich, $\geq 99.85\%$) for 8 hours to remove oxides and contaminants on the Cu surface. After loading the acid-treated Cu foil in the center of the furnace, the CVD system was first evacuated to $\sim 2 \times 10^{-2}$ torr for 10 min, followed by filling a gas mixture of Ar and H₂. Temperature was then ramped up to 1050 °C within 40 minutes to anneal the growth substrate (i.e., Cu foil). After annealing, the system was kept at 1050 °C, followed by introducing the CH₄ precursor into the reaction tube as a carbon source to initiate the graphene growth for 30 minutes. After reaction, both H₂ and CH₄ were turned off and the CVD system was cooled to room temperature under an Ar flow.

A polymethyl methacrylate (PMMA, MicroChem, 950 PMMA, A4) film was deposited on the as-grown monolayer graphene by spin coating to form a layered stack of PMMA/graphene/Cu. The PMMA/graphene/Cu was then dipped into Marble's solution (CuSO₄ : HCl : H₂O = 10 g : 50 mL : 50 mL) to etch away the Cu substrate, resulting in a PMMA/graphene stack suspending on the solution surface. Subsequently, the PMMA/graphene was transferred to deionized water to further remove the remaining etchants. A flexible G-FET device on a PI film was prepared by scooping up the floating PMMA/graphene stack in deionized water with a pair of pre-patterned source-drain electrodes of MLG-CuNPs. The thickness of the MLG-CuNP electrodes is ~ 100 nm as measured by AFM scan with the images shown in Figure S6. When bailing the PMMA/graphene out, care was taken to bridge the PMMA/graphene on the source-drain electrodes of MLG-CuNPs. Finally, after the PMMA was removed from PMMA/graphene by thermal annealing, a dielectric layer (30 nm-thick SiO₂) and a top-gate (10 nm Cr/50 nm Au) were deposited sequentially on top of the graphene by thermal evaporation at the deposition

rate of 1 Å/s to form a G-FET device (as illustrated in Figure 4c of the main text). The length and the width of the graphene channel are ~150 μm and ~500 μm, respectively.

The field-effect mobilities of the charge carriers (electrons and holes) in a G-FET device were calculated with the equation^{S11}

$$\mu_{FE} = \frac{dI_{ds}}{dV_{gs}} \times \frac{L}{W \times C_{ox} \times V_{ds}}$$

where L is the channel length, W is the channel width, $\frac{dI_{ds}}{dV_{gs}}$ is the slope of transfer curve of the G-FET device measured at $V_{ds} = 0.1$ V, and C_{ox} is the gate capacitance of 1.15×10^{-7} F/cm² for the 30 nm-SiO₂ dielectric layer. The values of $\frac{dI_{ds}}{dV_{gs}}$ for electrons and holes were obtained by fitting the transfer curve of the G-FET device.^{S10}

S4. MLG-CuNPs/CC as an electro-catalytic electrode in HER

Electrochemical measurements were conducted in a three-electrode electrochemical cell using a potentiostat/galvanostat (PGSTAT, FRA2 μAutolab TYPE III, Eco-Chemie, Utrecht, the Netherlands). All the electrochemical measurements were carried out in 1 M KOH electrolyte, which was purged with high-purity N₂ gas before use. One of our prepared electrodes (i.e., MLG-CuNPs/CC, CuNPs/CC, or MLG/CC), a platinum sheet, and an Ag/AgCl/sat'd KCl_(aq) reference electrode were employed as the working electrode, counter electrode, and reference electrode, respectively. The electro-catalysis was performed with a linear sweeping rate of 10 mV s⁻¹ in the voltage range of -600–100 mV (vs. the reversible hydrogen electrode (RHE)). Electrochemical impedance spectroscopy (EIS), operated in potentiostatic mode at -375 mV (vs. RHE), was scanned from 100 kHz to 10 mHz. The stability of electro-catalysts was tested via the continuous electrolysis at a fixed overpotential for a long-term operation.

S4.1. The structure and morphology of a CuNPs/CC electrode

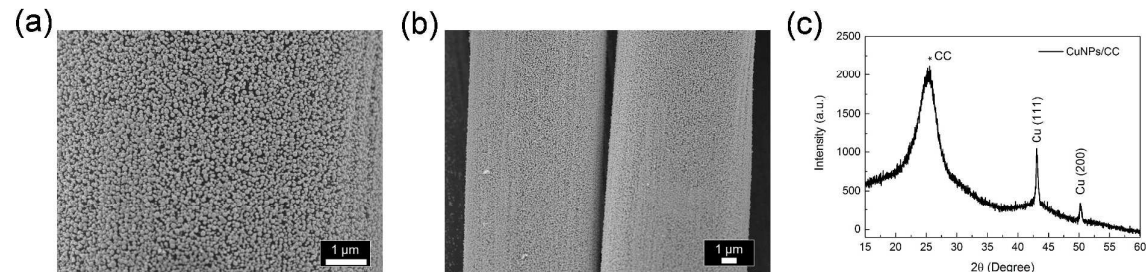


Figure S10. (a) High-magnification and (b) low-magnification SEM images of a CuNP/CC electrode. (c) The XRD pattern of a CuNPs/CC electrode.

S4.2. Collapsed MLG shells

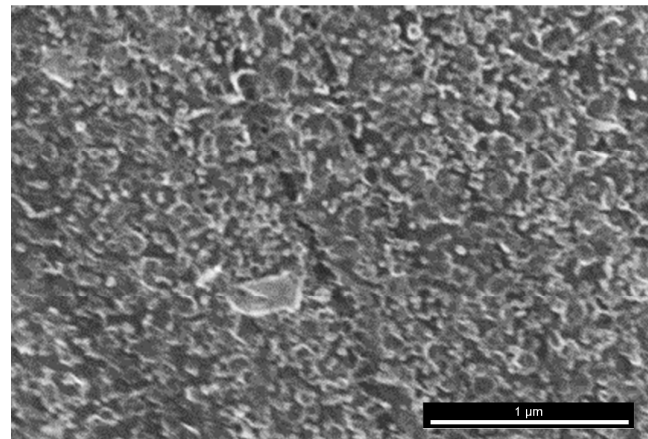


Figure S11. An SEM image of the collapsed MLG shells.

Table S2. A partial literature review of the HER performances of various copper-based electro-catalysts.

Electro-catalyst	Overpotential ^a (J_{cathodic})	Electrolyte	Durability test	Ref.
Cu film	-120 mV (1 mA cm ⁻²)	0.5 M PBS (pH 7.0)	8 h, at -350 mV (~6.25 mA cm ⁻²)	12
Cu nanoparticles	-450 mV (10 mA cm ⁻²)	0.5 M KOH	N.A.	13
Cu/Cu ₂ O	-160 mV (1 mA cm ⁻²)	0.5 M KPi (pH 7.0)	5 h, at -55 mV (~0.06 mA cm ⁻²)	14
Leaf-like hierarchical Cu	-150 mV (1 mA cm ⁻²)	0.1 M KPi (pH 7.0)	10 h, at -465 mV (~10 mA cm ⁻²)	15
Cu disk	-450 mV (1 mA cm ⁻²)	0.1 M KOH	N.A.	16
Cu nanoparticles	-400 mV (10 mA cm ⁻²)	0.5 M KOH	N.A.	17
Cu nanoparticles	-350 mV (0.05 mA cm ⁻²)	0.1 M HClO ₄	N.A.	18
Na[Cu(opba)]	-480 mV (1 mA cm ⁻²)	0.25 M PBS (pH 7.0)	N.A.	19

Cu[L]	-580 mV (1 mA cm ⁻²)	0.25 M PBS (pH 7.0)	N.A.	20
[(bztpen)Cu](BF ₄) ₂	-340 mV (1 mA cm ⁻²)	0.1 M PBS (pH 2.5)	N.A.	21
Cu(TPA)	-440 mV (1 mA cm ⁻²)	0.1 M KPi (pH 9.2)	>5 h, at -200 mV (~1.35 mA cm ⁻²)	22
MLG-CuNPs	-83 mV -375 mV (1 mA cm ⁻²); (10 mA cm ⁻²)	0.5 M KOH	18 h, at -375 mV (~10 mA cm ⁻²)	This work

^aPotential *vs.* RHE

Reference

- S1 Lee, S.; Hong, J.; Koo, J. H.; Lee, H.; Lee, S.; Choi, T.; Jung, H.; Koo, B.; Park, J.; Kim, H.; Kim, Y.-W.; Lee, T. Synthesis of Few-Layered Graphene Nanoballs with Copper Cores Using Solid Carbon Source. *ACS Appl. Mater. Interfaces* **2013**, *5*, 2432–2437.
- S2 Woo, Y. S.; Seo, D. H.; Yeon, D. H.; Heo, J.; Chung, H. J.; Benayad, A.; Chung, J. G.; Han, H.; Lee, H. S.; Seo, S.; Choi, J. Y. Low Temperature Growth of Complete Monolayer Graphene Films on Ni-Doped Copper and Gold Catalysts by a Self-Limiting Surface Reaction. *Carbon* **2013**, *64*, 315–323.
- S3 Zhang, B.; Lee, W. H.; Piner, R.; Kholmanov, I.; Wu, Y.; Li, H.; Ji, H.; Ruoff, R. S. Low-Temperature Chemical Vapor Deposition Growth of Graphene from Toluene on Electropolished Copper Foils. *ACS Nano* **2012**, *6*, 2471–2476.
- S4 Jacobberger, R. M.; Levesque, P. L.; Xu, F.; Wu, M.-Y.; Choubak, S.; Desjardins, P.; Martel, R.; Arnold, M. S. Tailoring the Growth Rate and Surface Facet for Synthesis of High-Quality Continuous Graphene Films from CH₄ at 750 °C via Chemical Vapor Deposition. *J. Phys. Chem. C* **2015**, *119*, 11516–11523.
- S5 Kim, C.; Lee, G.; Rhee, C.; Lee, M. Expeditious Low-Temperature Sintering of Copper Nanoparticles with Thin Defective Carbon Shells. *Nanoscale* **2015**, *7*, 6627–6635.
- S6 Deng, D.; Cheng, Y.; Jin, Y.; Qi, T.; Xiao, F. Antioxidative Effect of Lactic Acid-Stabilized Copper Nanoparticles Prepared in Aqueous Solution. *J. Mater. Chem.* **2012**, *22*, 23989–23995.
- S7 Tanuma, S.; Powell, C. J.; Penn, D. R. Calculations of Electron Inelastic Mean Free Paths. *Surf. Interface Anal.* **1991**, *17*, 911–926.
- S8 Biesinger, M. C.; Lau, L. W. M.; Gerson, A. R.; Smart, R. S. C. Resolving Surface Chemical States in XPS Analysis of First Row Transition Metals, Oxides and Hydroxides: Cr, Mn, Fe, Co and Ni. *Appl. Surf. Sci.* **2010**, *257*, 887–898.

- S9 Miller, D. J.; Biesinger, M. C.; McIntyre, N. S. Interactions of CO₂ and CO at Fractional Atmosphere Pressures with Iron and Iron Oxide Surfaces: One Possible Mechanism for Surface Contamination? *Surf. Interface Anal.* **2002**, *33*, 299–305.
- S10 Chen, C. C.; Kuo, C. J.; Liao, C. Da; Chang, C. F.; Tseng, C. A.; Liu, C. R.; Chen, Y. T. Growth of Large-Area Graphene Single Crystals in Confined Reaction Space with Diffusion-Driven Chemical Vapor Deposition. *Chem. Mater.* **2015**, *27*, 6249–6258.
- S11 Yu, X.; Dong, Z.; Liu, Y.; Liu, T.; Tao, J.; Zeng, Y.; Yang, J. K. W.; Wang, Q. J. A High Performance, Visible to Mid-Infrared Photodetector Based on Graphene Nanoribbons Passivated with HfO₂. *Nanoscale* **2016**, *8*, 327–332.
- S12 Du, J.; Wang, J.; Ji, L.; Xu, X.; Chen, Z. A Highly Active and Robust Copper-Based Electrocatalyst toward Hydrogen Evolution Reaction with Low Overpotential in Neutral Solution. *ACS Appl. Mater. Interfaces* **2016**, *8*, 30205–30211.
- S13 Kumar, B.; Saha, S.; Basu, M.; Ganguli, A. K. Enhanced Hydrogen/oxygen Evolution and Stability of Nanocrystalline (4–6 nm) Copper Particles. *J. Mater. Chem. A* **2013**, *1*, 4728–4735.
- S14 Zhao, J.; Tran, P. D.; Chen, Y.; Loo, J. S. C.; Barber, J.; Xu, Z. J. Achieving High Electrocatalytic Efficiency on Copper: A Low-Cost Alternative to Platinum for Hydrogen Generation in Water. *ACS Catal.* **2015**, *5*, 4115–4120.
- S15 Liu, X.; Cui, S.; Sun, Z.; Du, P. Robust and Highly Active Copper-Based Electrocatalyst for Hydrogen Production at Low Overpotential in Neutral Water. *Chem. Commun.* **2015**, *51*, 12954–12957.
- S16 Sheng, W.; Myint, M.; Chen, J. G.; Yan, Y. Correlating the Hydrogen Evolution Reaction Activity in Alkaline Electrolytes with the Hydrogen Binding Energy on Monometallic Surfaces. *Energy Environ. Sci.* **2013**, *6*, 1509–1512.
- S17 Kumar, B.; Saha, S.; Ganguly, A.; Ganguli, A. K. A Facile Low Temperature (350 °C)

- Synthesis of Cu₂O Nanoparticles and Their Electrocatalytic and Photocatalytic Properties. *RSC Adv.* **2014**, *4*, 12043–12049.
- S18 Björketun, M. E.; Bondarenko, A. S.; Abrams, B. L.; Chorkendorff, I.; Rossmeisl, J. Screening of Electrocatalytic Materials for Hydrogen Evolution. *Phys. Chem. Chem. Phys.* **2010**, *12*, 10536-10541.
- S19 Fu, L.-Z.; Fang, T.; Zhou, L.-L.; Zhan, S.-Z. A Mononuclear Copper Electrocatalyst for Both Water Reduction and Oxidation. *RSC Adv.* **2014**, *4*, 53674–53680.
- S20 Cao, J. P.; Fang, T.; Fu, L. Z.; Zhou, L. L.; Zhan, S. Z. First Mononuclear copper(II) Electro-Catalyst for Catalyzing Hydrogen Evolution from Acetic Acid and Water. *Int. J. Hydrogen Energy* **2014**, *39*, 13972–13978.
- S21 Zhang, P.; Wang, M.; Yang, Y.; Yao, T.; Sun, L. A Molecular Copper Catalyst for Electrochemical Water Reduction with a Large Hydrogen-Generation Rate Constant in Aqueous Solution. *Angew. Chemie - Int. Ed.* **2014**, *53*, 13803–13807.
- S22 Liu, X.; Zheng, H.; Sun, Z.; Han, A.; Du, P. Earth-Abundant Copper-Based Bifunctional Electrocatalyst for Both Catalytic Hydrogen Production and Water Oxidation. *ACS Catal.* **2015**, *5*, 1530–1538.